

# Mirau correlation microscope

Gordon S. Kino and Stanley S. C. Chim

We have constructed a correlation microscope based on the Mirau interferometer configuration using a thin silicon nitride film beam splitter. This microscope provides the amplitude and phase information for the reflected signal from a sample located on the microscope-object plane. The device is remarkably insensitive to vibrations and is self-correcting for spherical and chromatic range aberrations of the objective. An imaging theory for the correlation microscope has been derived, which predicts accurately both the transverse resolution at a sharp edge and the range resolution for a perfect plane reflector. The range resolution is slightly better than that for a scanning optical microscope using a lens with the same aperture.

## I. Introduction

We have constructed a device we call the Mirau correlation microscope (MCM) which is based on the Mirau interferometer configuration. The basic idea is to employ an interferometric microscope with a spatially and temporally incoherent light source and to use as the detected output the correlation signal between the beams reflected from the object and from a reference mirror, respectively. The device has a transverse and range resolution comparable with or better than the confocal scanning optical microscope (CSOM)<sup>1</sup> or real time scanning optical microscope (RSOM)<sup>2</sup> and is capable of measuring both amplitude and phase. Because this information is available in the computer associated with the device, it is relatively easy to use Fourier transform techniques to modify the spatial frequency response of the microscope in both the range and transverse directions.

The basic idea behind this system is similar to that of the coherence microscope described by Davidson *et al.*<sup>3</sup> Their system, which uses a Michelson interferometer and is based on the Leitz Linnik microscope configuration, is shown in Fig. 1. We shall describe first the principles of the coherence microscope and how we have changed the design to use a Mirau interferometer rather than a Michelson interferometer. We then describe the experiments carried out to measure amplitude and phase and explain how we obtained images with a wide variety of samples using the Mirau correlation microscope.

In the Linnik microscope, a spatially and temporally incoherent light source from a filament lamp or xenon

arc lamp passes light through a condenser and the objective lens to the sample being observed. Part of the light passes through a beam splitter and an identical objective lens to a plane mirror, the reference in the Michelson interferometer. Light from the object and reference mirror passes back through the beam splitter to a CCD detector array. The two signals *A* from the object and *B* from the reference mirror interfere at the detector if their beam paths are almost identical.

The output current *I* from the detector is of the form

$$I = A^2 + B^2 + 2AB\gamma(z - z_0), \quad (1)$$

where *z* is the distance of the reflecting point from the focus, and *z*<sub>0</sub> is the distance of the reference mirror from the focus, while  $\gamma(z)$  is the autocorrelation function for the broadband spatially incoherent light source. In Davidson's system as well as our own, the detected signal is electronically processed to keep only the product term and the envelope of  $\gamma(z)$ . The autocorrelation function  $\gamma(z)$  is controlled by both the spatial and temporal coherence of the source.

One advantage of this microscope is that it tends to remove spherical and chromatic aberrations of the objective in the *z*-direction, which we shall refer to as range aberrations; this is because identical lenses are used in the reference and beam paths. Its disadvantages are that, because of the electronic processing required, it is relatively slow compared to the RSOM. It also needs two identical objectives, and, because of the long beam paths involved, it must be built massively to avoid vibration problems.

Our design, shown in Fig. 2, overcomes some of these disadvantages. Instead of a Michelson interferometer, a Mirau interferometer consisting of a beam splitter and reference mirror is positioned between the objective and sample. The difficulty with this arrangement is that the beam splitters in a Mirau interferometer can introduce severe aberrations in a wide aperture system. The spherical aberration in the *z*-

The authors are with Stanford University, Hansen Laboratories of Physics, Ginzton Laboratory, Stanford, California 94305-4085.

Received 19 December 1989.

0003-6935/90/263775-09\$02.00/0.

© 1990 Optical Society of America.

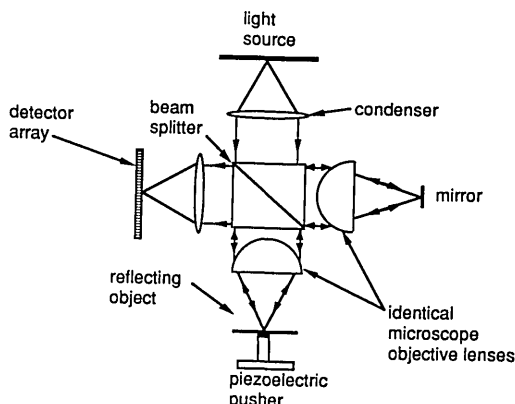


Fig. 1. Linnik correlation microscope.

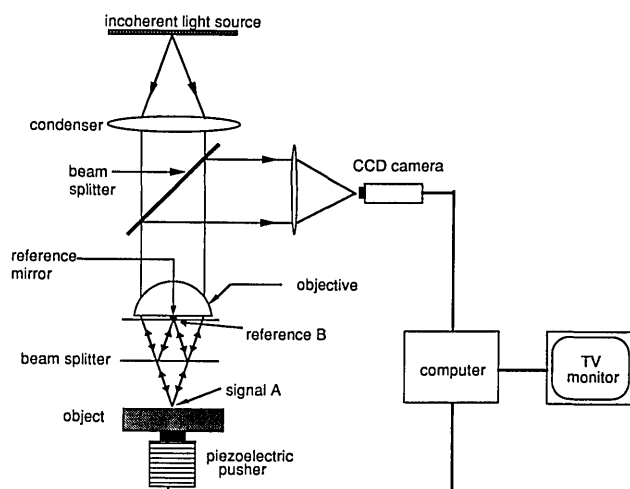


Fig. 2. Mirau correlation microscope.

direction increases approximately as the cube of the numerical aperture. Therefore, it has not been possible to construct a wide aperture interferometric microscope with a Mirau interferometer using the standard plastic film pellicle beam splitters, which are typically of the order of  $3\ \mu\text{m}$  thick. To avoid this difficulty, we constructed a beam splitter using a low stress film of silicon nitride, which is only  $800\ \text{\AA}$  thick, and the reference mirror is built by depositing a platinum disk on a silicon nitride film. These films are made by depositing silicon nitride on silicon and then etching a hole in the silicon. They introduce very little aberration into a  $0.8$  aperture beam and are suitable for beam splitters with an  $\sim 50\%$  split in power, which is what we need.<sup>4</sup>

The reference mirror is always kept at the focal plane  $z = z_0$  of the objective, while the sample is scanned along the vertical axis ( $z$ -axis) by a computer-controlled piezoelectric pusher which determines the vertical location of the sample. Initial adjustment of the position of the two films is made by means of a vernier screw system along with an electronically controlled piezoelectric pusher. A CCD camera is used to

obtain image signals which can be inserted into a computer for further processing.

The reference and sample beams share a common path over most of their length. Hence this system is much less sensitive to vibration than the Linnik configuration. In addition, only one lens is required, although this lens must have a relatively long working distance to accommodate the beam splitters. In our case we used a Leitz  $0.8$  aperture lens with a working distance of  $2\ \text{mm}$ . It is also possible to construct this type of microscope with a  $0.9$  aperture lens with a working distance of  $1\ \text{mm}$ .

## II. Theory

### A. Response of the Microscope to a Planar Reflector

We first consider the response of the microscope to a planar reflector at a distance  $z$  from the focus. Let the incident waveform at the focal plane be  $u(x,y)$  and its spatial Fourier transform be

$$U(k_x, k_y) = \int_{-\infty}^{\infty} u(x,y) \exp[-j(k_x x + k_y y)] dx dy. \quad (2)$$

The reflected wave component  $U_S(k_x, k_y)$  from the object, which is assumed to be a distance  $z$  from the front surface of the objective, can be written as

$$U_S(k_x, k_y) = BU(-k_x, -k_y) \exp[-j(2k_z z + \phi)], \quad (3)$$

where  $\phi$  is the phase change on reflection from the object. The reflected wave component  $U_R(k_x, k_y)$  from the reference mirror at the reference focal plane  $z = z_0$  is of the form

$$U_R(k_x, k_y) = AU(-k_x, -k_y) \exp(-2jk_z z_0), \quad (4)$$

where  $A(k_x, k_y)$  and  $B(k_x, k_y)$  are parameters proportional to the reflection coefficient from the planar object and reference mirror, respectively. We can write in cylindrical coordinates  $k_z = \sqrt{k^2 - k_x^2 - k_y^2} = k \cos \theta$ ,  $k_r = \sqrt{k_x^2 + k_y^2} = k \sin \theta$ , where  $\theta$  is the angle of the ray to the axis with a wave of propagation constant  $k_r, k_z$  propagating along it. It is assumed that  $|U(k_x, k_y)|$  is constant for  $\theta \leq \theta_0$  and zero for  $\theta > \theta_0$ , where the numerical aperture of the objective is  $\text{N.A.} = \sin \theta_0$ .

The output current from the detector is of the form

$$\begin{aligned} i(z) &= 2\pi \int |U_R + U_S|^2 k_r dk_r \\ &= 4\pi k^2 |U|^2 \int_0^{\theta_0} \{A^2 + B^2 + 2AB \cos[2k(z - z_0) + \phi]\} \\ &\quad \times \sin \theta \cos \theta d\theta. \end{aligned} \quad (5)$$

We are concerned mainly with the correlation term or product term  $AB$  in the integrand. When the illumination is of a finite bandwidth with an intensity variation  $F(k)$ , the correlation term is then given by the relation

$$\begin{aligned} I_{AB}^b(z) &= 4\pi AB |U|^2 \int_{\text{bandwidth}} \int_0^{\theta_0} k^2 \\ &\quad \times [\cos[2k(z - z_0) \cos \theta + \phi] \sin \theta \cos \theta d\theta] F(k) dk, \end{aligned} \quad (6)$$

where the superscript  $b$  stands for broadband.

When  $\phi = 0$  or  $\pi$ , the term  $I_{AB}^b(z)$  is roughly a sinusoi-

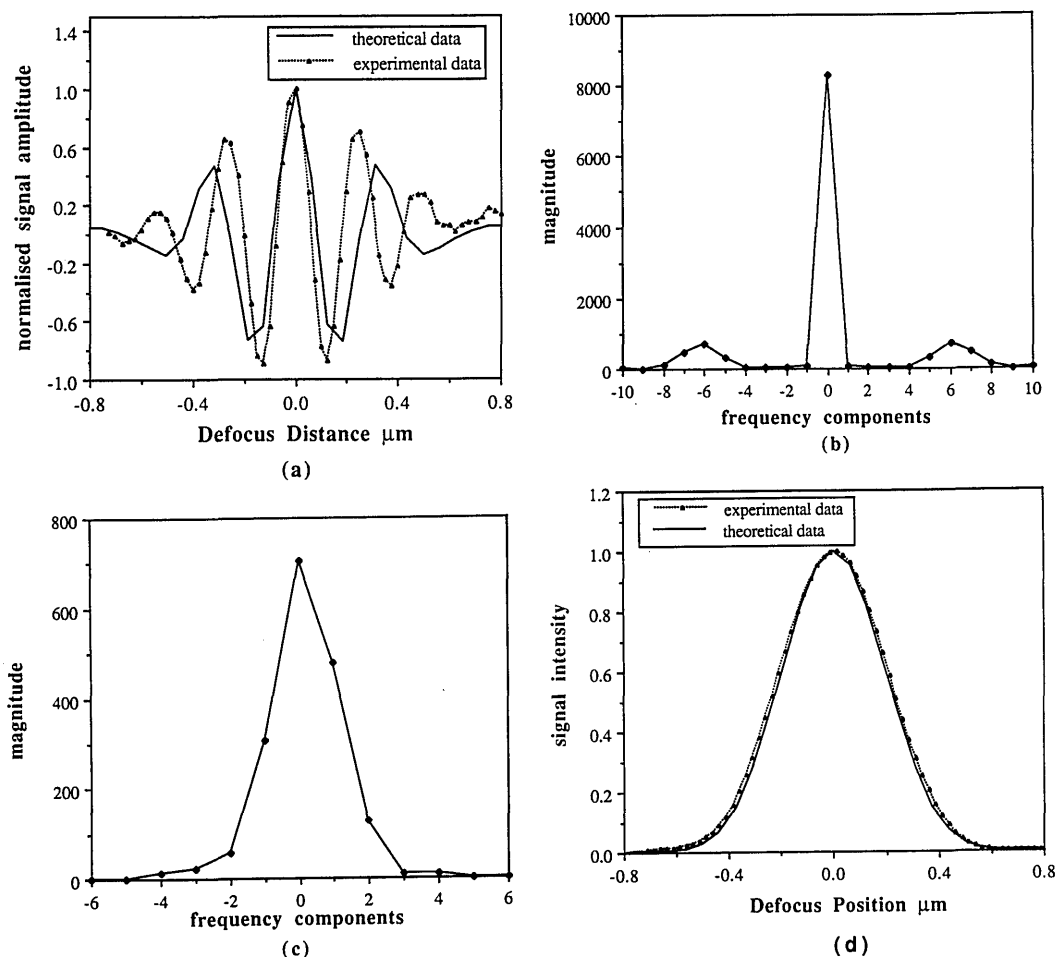


Fig. 3. Filtering process in the Fourier domain: (a) raw data from the detector; (b) magnitude of the individual frequency components in the Fourier domain; (c) filtering in the Fourier domain to eliminate the negative frequencies and centering the positive frequency packet, as shown; (d) transformed data from inverse Fourier transforming the frequency packet in (c).

dal variation modified by an envelope which has a maximum at  $z = 0$  and falls off monotonically with  $|z - z_0|$ , i.e., like a modulated carrier, as shown in Fig. 3(a). We wish to keep only the envelope of this function so as to obtain an unambiguous monotonic variation of output amplitude with  $z - z_0$ . We do this by taking measurements at sixty-four values of  $z$ , carrying out a Fourier transform in the  $z$ -dimension, and eliminating the negative spatial frequencies. It is often convenient to center the packet of positive spatial frequency components to lower the spatial frequencies in the transform as much as possible, as shown in Figs. 3(b) and (c). After this process is carried out, the inverse Fourier transform is taken to yield both the amplitude and phase of the signal. The resulting complex transformed signal, when centering is not carried out, has the form

$$I_{AB}^{bp}(z) = 4\pi AB|U|^2 \int_{\text{bandwidth}} \int_0^{\theta_0} k^2 \times (\exp\{-j[\phi + 2k(z - z_0) \cos\theta]\} \sin\theta \cos\theta d\theta) F(k) dk, \quad (7)$$

where the superscript  $p$  stands for a processed signal.

The magnitude of the function  $I_{AB}^{bp}(z)$  is plotted in Fig. 3(d).

It should be noted that it is the square of this function which corresponds to and should be compared with the detector output or intensity of a standard microscope or a confocal microscope. The correlation microscope by its nature uses coherent detection, and the output is proportional to the amplitude of the signal rather than its intensity. For the same reason, the correlation microscope has much better sensitivity to weak reflectors than a standard microscope, because the output is proportional to the signal amplitude  $A$  rather than intensity  $A^2$ . Thus the correlation microscope should be particularly useful for observing small defects and dust particles on semiconductor structures and weak reflectors inside biological materials.

## B. Range Resolution

The range resolution of the microscope can be found for single frequency excitation in just the same way as for the confocal microscope. For narrowband excita-

tion with  $\phi = 0$ , if we write  $F(k) = \delta(k_0)$ , where  $\delta(k_0)$  is a  $\delta$ -function, it follows that Eq. (7) takes the form

$$I_{AB}(z) = 2AB|W|^2 \int_0^{\theta_0} \exp[-2jk_0(z - z_0)] \sin\theta \cos\theta d\theta. \quad (8)$$

This formula is identical to that for the amplitude variation with distance  $z$  of the confocal microscope. For a narrowband system, the variation of the output signal from the detector (which is proportional to the amplitude) is identical to the amplitude variation with distance  $z$  of the wave passing through the pinhole of a confocal scanning optical microscope.<sup>1,2,5</sup> Following that analysis, using the paraxial assumption  $\cos\theta \approx 1$  with  $\phi = 0$  for simplicity, the signal output normalized to its amplitude at  $z = z_0$  is

$$I(z) = \frac{\sin[k_0(z - z_0)(1 - \cos\theta_0)]}{k_0(z - z_0)(1 - \cos\theta_0)} \times \exp[-jk_0(z - z_0)(1 + \cos\theta_0)]. \quad (9)$$

It will be observed that if a spatial Fourier transform in the coordinate  $(z - z_0)$  is taken of this expression, the result would be like that for a carrier with a spatial frequency  $k_0(1 + \cos\theta_0)$ , modulated by a square topped pulse of width  $\Delta k = k_0(1 - \cos\theta)$ . The original output from the detector, if a narrowband source were used, would have two modulated carriers and a strong dc component corresponding to the  $A^2 + B^2$  term in Eq. (5).

For narrowband excitation, the resulting range resolution between half power points [half the maximum value of  $I^2(z)$ ] is

$$d_z = \frac{0.45\lambda}{1 - \cos\theta_0}, \quad (10)$$

where  $k_0 = 2\pi/\lambda$  and  $\lambda$  is the optical wavelength. For a 0.8 aperture lens, this formula is in error by only 1% from the exact formula derived from Eq. (8).<sup>5</sup>

For a broadband source centered at a frequency corresponding to  $k_0$  and with uniform illumination over a wavenumber bandwidth  $\Delta k$ , the envelope  $g(z)$  or the correlation function  $\gamma(z)$  is given by the relation

$$g(z - z_0) = \frac{\sin\left[\frac{\Delta k}{2}(z - z_0)(1 + \cos\theta_0)\right]}{\frac{\Delta k}{2}(z - z_0)(1 + \cos\theta_0)}. \quad (11)$$

Thus, with a broadband source, even if the aperture of the lens were small, the range resolution between half power points would be limited by the bandwidth to

$$d_z = \frac{1.78\pi}{\Delta k(1 + \cos\theta_0)}. \quad (12)$$

More generally with finite bandwidth and a finite aperture, the range resolution is smaller than its value due to either effect alone. One explanation for this effect is based on the spatial frequency response in the  $z$ -direction.<sup>6</sup> When a single frequency ray at the maximum angle  $\theta_0$  to the axis is reflected at the mirror angle from a planar substrate, the total change in wavenumber is  $\delta k_z = 2k_0 \cos\theta_0$ . However, the change in wavenumber for the reflected on-axis rays is  $\delta k_z = 2k_0$ .

Therefore, the maximum range of spatial frequencies available is  $\Delta k_z = 2k_0(1 - \cos\theta_0)$ . Integration over all angles  $\theta$ , as we discussed after Eq. (9), shows that the effective value of  $\Delta k_z$  for single frequency rays is  $\Delta k_z = k_0(1 - \cos\theta_0)$ . If, in addition, the illumination bandwidth corresponds to a range of wavenumbers  $\Delta k$ , the range of spatial frequencies in the  $z$ -direction is increased by  $\delta k_z = \Delta k$ . Hence, summing the two effects, the total spatial frequency range is

$$\Delta k_z = 2k_1(1 - \cos\theta_0) + 2\Delta k = 2k_0(1 - \cos\theta_0) + \Delta k(1 + \cos\theta_0), \quad (13)$$

where the wavenumbers  $k_1$  and  $k_0$  are taken to correspond, respectively, to the lowest frequency and center frequency. With a more exact treatment, the effects of increase in aperture and bandwidth do not add directly, but there is a decrease in range resolution due to both causes.

Experimental and numerically calculated results illustrating this phenomenon are discussed in the experimental section of this paper.

### C. Phase Measurements

An important feature of the correlation microscope is that, because there is a reference present, it can give a direct measurement of phase. It can be seen from Eq. (6) and Fig. 3(a) that the direct output from the microscope as the object is moved in the  $z$ -direction exhibits a series of fringes or maxima and minima. The peak of the envelope of  $I_{AB}^b(z)$ , or the maximum amplitude of the product signal  $AB$ , occurs when the reference and sample path lengths are the same; at the plane  $z = z_0$ . In Fig. 4, we plot the detected intensity as a function of position  $z_s$  in sample coordinates  $(x_s, y_s, z_s)$  for a 0.1- $\mu\text{m}$  tall step. This coordinate system is fixed to the sample and thus moves with respect

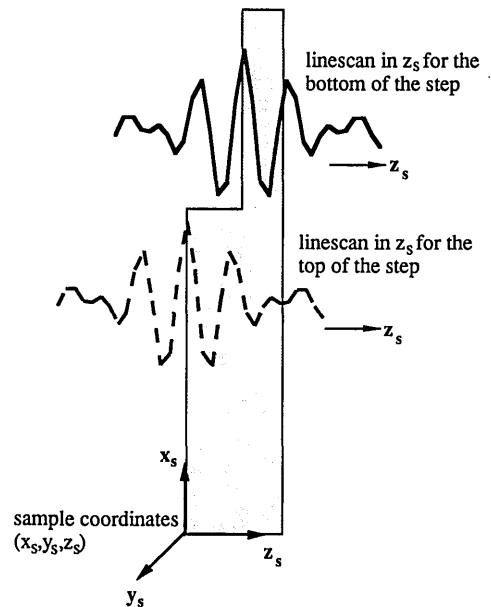


Fig. 4. Detected signals in same coordinates  $(x_s, y_s, z_s)$ .

to the microscope as the sample is scanned in the  $z$ -direction, where  $z$  is a coordinate based on the frame of the microscope. As the sample is scanned in  $z$ , areas of different height  $h(x_S, y_S)$  are independently imaged as they pass through the focal plane  $z = z_0$ . Two different curves are plotted on this graph; the dotted line is the  $I(z_S)$  curve for the top of the step, while the solid line is the  $I(z_S)$  curve for the bottom of the step. In Fig. 4, the position of the peak defines the profile of the object. To obtain phase information for a narrowband system, Eq. (9) can be rewritten in sample coordinates as

$$I(z_S) = \frac{\sin[k_0(z_S - h(x_S, y_S))](1 - \cos\theta_0)}{k_0(z_S - h(x_S, y_S))(1 - \cos\theta_0)} \times \exp[-jk_0(z_S - h(x_S, y_S))(1 + \cos\theta_0)]. \quad (14)$$

The height of the step can be accurately determined by Fourier transforming the data in Fig. 4 with respect to  $z_S$ . When the data are transformed, as we have described, the spatial frequency components are downshifted by  $k_0(1 + \cos\theta_0)$ . In the space domain this operation is equivalent to multiplying the phase term in Eq. (13) by  $\exp[jk_0(1 + \cos\theta_0)z_S]$ . The resulting phase shift is thus

$$\varphi = k_0(1 + \cos\theta_0)h(x_S, y_S). \quad (15)$$

The concept can be generalized to finite bandwidth illumination, and the phase of the final signal obtained [see Eq. (7)] can be related to the sample profile  $h(x_S, y_S)$ . Alternatively, measurement of the profile can be made by determining the shift of a minimum or maximum of the signal received at the detector as the beam is scanned over the profile of the sample.

#### D. Transverse Resolution

The transverse resolution can be found by standard imaging theory as has been done by Davidson.<sup>3</sup> Propagating back to the image plane of the objective, which is labeled by the coordinates  $(x_i, y_i)$ , the reference wave  $u_R(x_0, y_0)$  and the wave from the object  $u_S(x, y)$  become, respectively;<sup>7</sup>

$$u_R(x_i, y_i) = \int h(x_0 - x_i, y_0 - y_i)u_R(x_0, y_0)dx_0dy_0, \quad (16)$$

$$u_S(x_i, y_i) = \int h(x - x_i, y - y_i)u_S(x, y)dx dy, \quad (17)$$

where  $h(x, y)$  is the point spread function of the objective.

The signal detected by the CCD camera is  $|\langle u_R + u_S \rangle|^2$ . The cross product or the correlation term of the detected signal is  $2|u_R(x_i, y_i)u_S(x_i, y_i)|$ , where

$$\begin{aligned} |u_R(x_i, y_i)u_S(x_i, y_i)| \\ = \int \int |h(x - x_i, y - y_i)h(x_0 - x_i, y_0 - y_i) \\ \times \langle u_R(x_0, y_0)u_S(x, y) \rangle| dx dy dx_0 dy_0. \end{aligned} \quad (18)$$

For a spatially incoherent source,  $|\langle u_R(x_0, y_0)u_S(x, y) \rangle|$  is zero unless  $(x_0, y_0)$  and  $(x, y)$  are identical. The correlation term for an object in the focal plane can then be simplified to the form

$$I_{AB}(x_i, y_i) = \int 2AB|h(x - x_i, y - y_i)|^2 dx dy. \quad (19)$$

This expression is linear in signal amplitude  $A$ . Thus the amplitude point spread function of the microscope is  $|h(x, y)|^2$ , and, therefore, the intensity point spread function for a point object is given by  $|h(x, y)|^4$ , as it is for the confocal microscope. For a cylindrically symmetric paraxial system, the normalized value of  $h(r)$  is given for a paraxial system by the relation

$$h(r) = \frac{J_1(2\pi r/\lambda \sin\theta_0)}{\pi r/\lambda \sin\theta_0}. \quad (20)$$

This theory can be modified to take account of the finite bandwidth and the use of a nonparaxial system. The finite bandwidth tends to lower the level of the outer sidelobes but does not much affect the width of the main lobe if this width is calculated by using the midband frequency of the light; the elimination of the paraxial assumption tends to widen the main lobe slightly.

### III. Experimental Results

#### A. Measurement of the Intensity Response $I(z)$

In our experiment, a bare silicon wafer is scanned in the  $z$ -direction, and the raw amplitude response is plotted in Fig. 3(a). For comparison with theory, to reproduce the experimental conditions, we have assumed a cosine variation for  $F(k)$  with its zeros at wavelengths of 400 and 800 nm. The data are then transformed, as already described, to give the intensity response in Fig. 3(d). The corresponding theoretical results are also plotted in Figs. 3(a) and (d). The experimental intensity response of Fig. 3(d), which is the square of the magnitude of the amplitude signal, agrees well with theory; the measured half power width is  $0.49 \mu\text{m}$ , while the theoretical value is  $0.46 \mu\text{m}$ . The agreement between the experimental and theoretical raw amplitude responses in Fig. 3 is good on the main lobe but deteriorates at the outer sidelobes. This is probably because our simple approximation to the frequency response of the system is imperfect.

To characterize the effects of the illumination bandwidth on the intensity response  $I(z)$ , high pass (or blue color) filters are introduced to limit the source bandwidth. A silicon wafer was scanned in the  $z$ -axis, and the range resolution  $d_z$  between half power points with three different filters in place was recorded. In Fig. 5 a plot is given of the experimental results (circles) as a function of bandwidth; these results are calculated by assuming that the glass components cut off at 400 nm. A theoretical comparison is made in the same plots by assuming in Eq. (6) a rectangular illumination spectrum with its lower cutoff wavelength at 420 nm. Although our set of experimental and empirical data does not coincide due to the oversimplified frequency spectrum assumed in numerical calculations, they are remarkably close in shape. Both range resolutions decrease approximately linearly with increase in bandwidth.

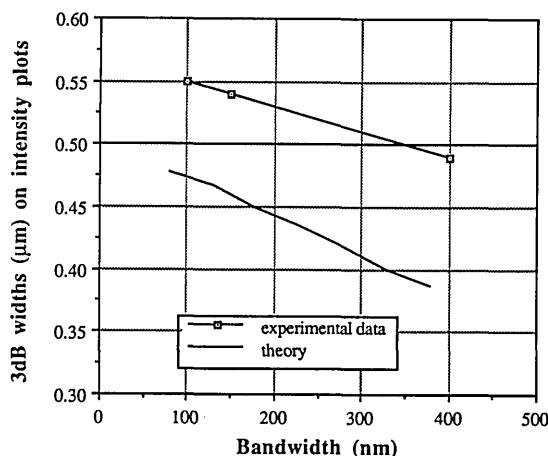


Fig. 5. Three-decibel width of the intensity scans plotted as a function of the bandwidth of the illumination spectrum.

### B. Measurement of the Edge Response

To characterize the transverse spatial response of the correlation microscope, a line scan was taken across a cleaved silicon sample which was assumed to be a perfect edge. The theoretical shape is the convolution of a perfect edge with the point spread function of the microscope; this has a theoretical 10–90% width of  $0.47\lambda/\text{N.A.}$ , where  $\lambda$  is the wavelength and N.A. is the numerical aperture of the objective. For the 0.8-N.A. objective used in the experiment and a peak CCD camera response at 550-nm wavelength, the calculated width is  $0.323\text{ }\mu\text{m}$ . Figure 7 shows an experimental edge scan with a 10–90% width of  $0.37\text{ }\mu\text{m}$ . As discussed above, the measured width is expected to be slightly wider than the theoretical value.

This microscope is capable of recording both the phase and amplitude of the reflected signal from an object, which makes it possible to design digital filters for extracting and enhancing features of interest. The Fourier transform of the microscope amplitude line spread function  $s(x) = |h(x)|^2$  is a transfer function  $S(k_x)$ , which is generally triangular in shape as illustrated in Fig. 6. This amplitude function contains twice the spatial bandwidth of a standard microscope, but the higher spatial components are suppressed, which minimizes the contributions by the high frequencies. One way to boost the higher spatial components in the signal is by inverse filtering. To avoid excessive noise amplification in regions where the signal level is low and the amplification is large, the inverse filter  $1/S(k_x)$  is tapered by a cosine function at the higher frequency regions.<sup>8</sup> Weighting the modified inverse function by the SNR, we obtain a modified Wiener filter which sharpens the edges without introducing excessive noise amplification. The dotted edge line scan in Fig. 7 shows the result of applying such a filter to the original amplitude and phase edge line scan data. The 10–90% width is reduced by more than 30% to  $0.23\text{ }\mu\text{m}$ , which is comparable to resolutions which could be obtained with near UV illumination.

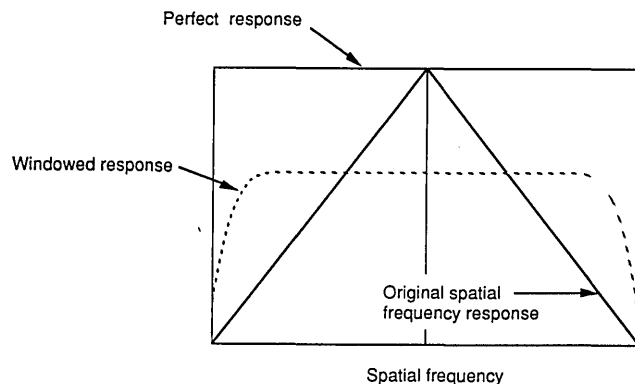


Fig. 6. Spatial frequency response of the correlation microscope compared with the perfect response. The optimized windowed response is shown as a dotted line.

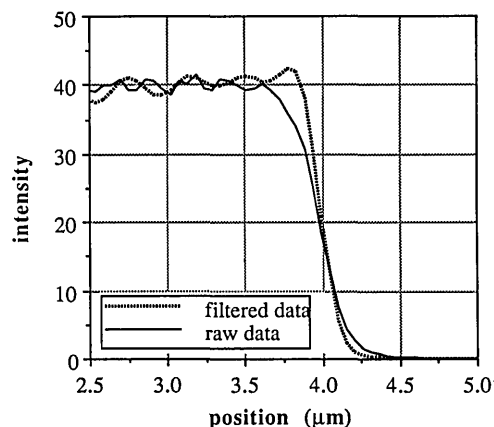


Fig. 7. Measured and filtered edge responses.

### C. Phase Measurements

As with other phase measuring microscopes, we can also use phase information to measure heights and widths of gratings with a thickness much less than the depth of resolution of the microscope.<sup>8</sup> For a single frequency parallel beam of wavenumber  $k_0 = 2\pi/\lambda$  reflected from a plane surface a distance  $\Delta z$  from a reference plane (in our case the focus), the change in phase  $\varphi$  of the beam is  $\Delta\varphi = 2k_0\Delta z$ . With a focused beam converging at an angle  $\theta_0$  to the optic axis, it is shown in Eq. (13) that  $\Delta\varphi = k_0\Delta z(1 + \cos\theta_0)$ .

We measured a 321-MHz surface acoustic wave resonator, supplied by Hewlett-Packard, which is in the form of a quartz grating  $2.4\text{ }\mu\text{m}$  wide and  $1050\text{ }\text{\AA}$  tall. Since the tops and bottoms of the grating have the same reflectivities, and its height is less than the range resolution, amplitude measurements do not provide much information on height. However, the correlation microscope records the signal phase as well as the amplitude. Figure 8 shows a measured phase line scan across the grating. The phase difference between the top and bottom of the grating is  $1.9\text{ rad}$ . In our system, the light source is broadband, and the CCD camera response peaks at a wavelength of 550 nm. Picking a

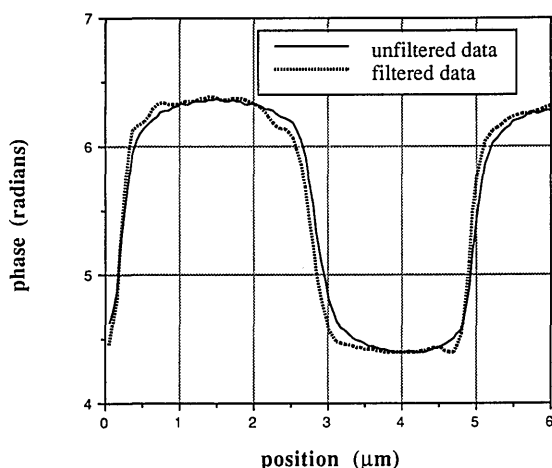


Fig. 8. Phase line scan across the SAW-321 resonator showing both the raw and filtered data.

wavelength of 550 nm and with a 0.8-N.A. objective, Eq. (13) gives a calculated height of 1040 Å from the measured phase difference. This deviation is only 10 Å from the nominal height suggested by the manufacturer. With the recorded amplitude and phase, the data have also been deconvolved, as already described, and the filtered phase line scan is plotted as a dotted line in Fig. 8. It will be seen that the line scans are sharpened slightly, and there is a flatter response over the top and bottom surfaces, thus making the phase measurement more accurate for narrower width samples.

#### D. Photoresist Trench Measurements

In integrated circuit manufacturing, photolithography is a common step to define patterns on chips. The profile of the photoresist structures and especially the dimensions of the regions cleared of photoresist after lithography are crucial in determining the active region for the following processing step. In this experiment we measure widths of isolated trenches etched in photoresist, which is spun on a bare silicon wafer for process control purposes. The photoresist is 1.25  $\mu\text{m}$  thick, and the width of the trenches varies from 0.4 to 1.1  $\mu\text{m}$  in increments of 0.1  $\mu\text{m}$ . The bottom of these trenches is measured, and the data are then processed by the Fourier transform technique as described. Figure 7 shows the intensity line scans (solid lines) across the bottom of the 1.0-, 0.7-, and 0.4- $\mu\text{m}$  wide trenches. The central peak locates the trench with respect to the wafer, and its width can be used as a measure of the actual width at the bottom of the trench. Outside the trench the signal contributed by the reflection from the surrounding photoresist is suppressed due to the shallow depth of focus.

With the correlation microscope, it is also possible to measure the phase across the bottom of the trenches, shown as dotted lines in Fig. 9. These phase scans have a W shape. At the outer sides of the W at the

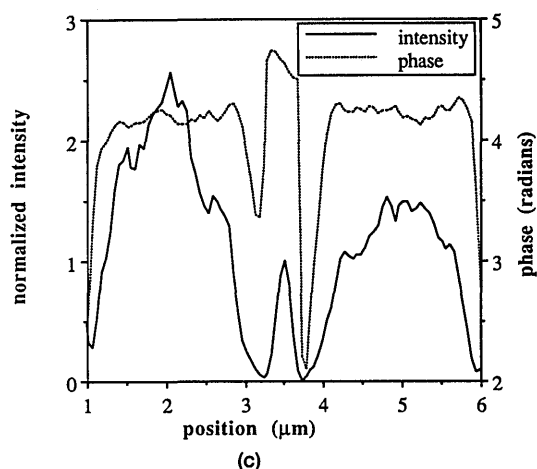
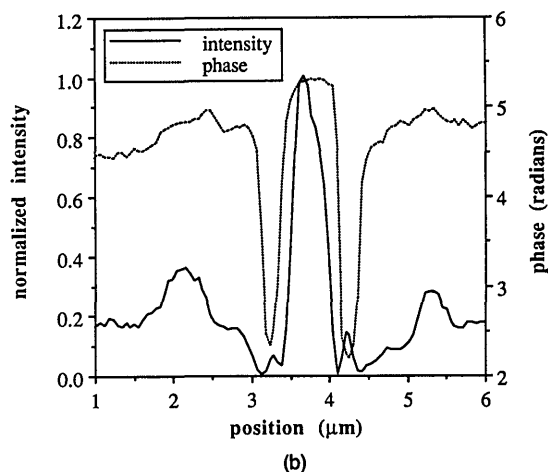
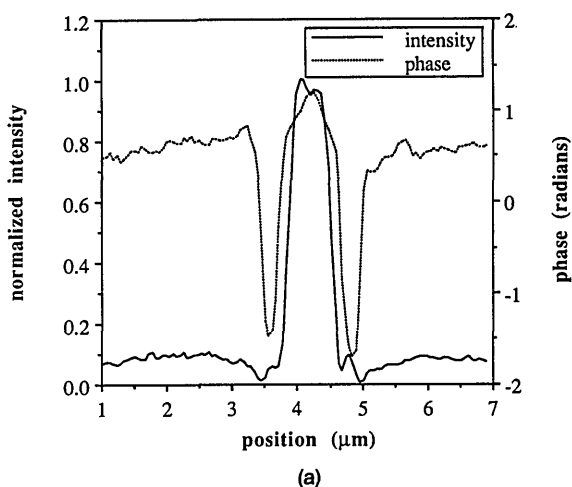


Fig. 9. Intensity and phase line scans across the bottom of the photoresist trenches 1.25  $\mu\text{m}$  thick of different widths: (a) 1.0- $\mu\text{m}$  wide trench; (b) 0.7- $\mu\text{m}$  wide trench; (c) 0.4- $\mu\text{m}$  wide trench.

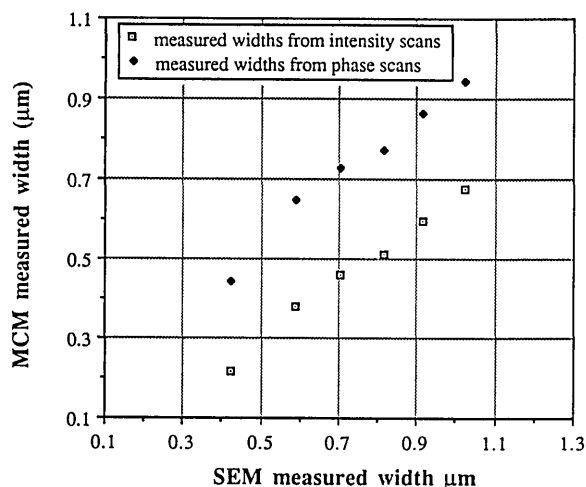
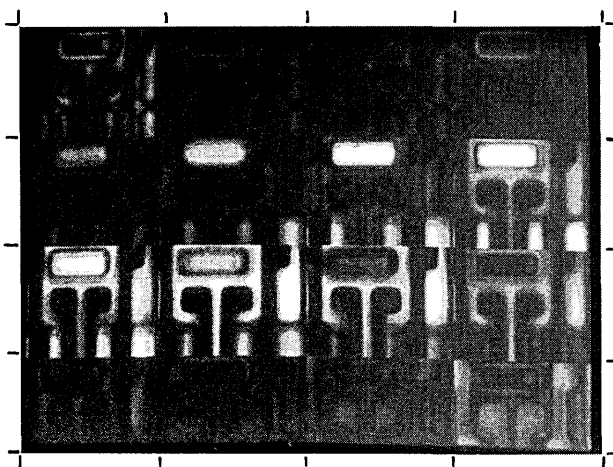


Fig. 10. Comparison between the MCM measurements and SEM measurements for the photoresist trenches.

edge of the trench is a signature arising from the discontinuity of the vertical photoresist walls and the bare silicon underneath. The bottom of the W again locates the trenches while the distance halfway up the outer edge of the W can be used as yet another measure of the actual width at the trench bottom.

Figure 10 shows a comparison between the widths of the trench bottom measured by the correlation microscope and by a scanning electron microscope. The widths as plotted are defined by the distance between the half power points on the central peak for the intensity scans and the distance at half the maximum phase excursions for the phase scans. The linear dependence of the measured widths and widths as measured by the SEM suggests that, after an initial calibration, the Mirau correlation microscope is capable of measuring submicron linewidths with accuracies comparable with a SEM.

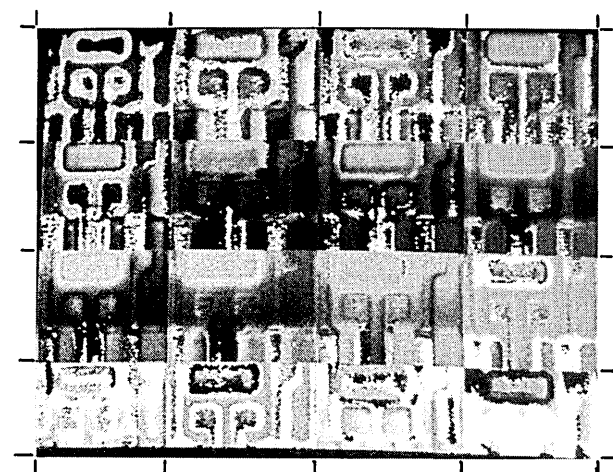
Bottom Focus



Top Focus

(a)

Bottom Focus



Top Focus

(b)

Fig. 11. (a) Sixteen cross-sectional intensity images of an integrated circuit at different foci. The axial separation of each image is  $0.137 \mu\text{m}$  along the z-axis. (b) Corresponding phase images of the same integrated circuit.



#### E. Two-Dimensional Cross-Sectional Images of an Integrated Circuit

To illustrate the reconstruction of 2-D cross-sectional images from the raw data, a silicon integrated circuit was scanned along the  $z$ -axis for a distance of  $2.2\text{ }\mu\text{m}$ . Images were grabbed at sixty-four equally spaced vertical positions of the circuit and then processed by the Fourier transform algorithm as described. Figure 11(a) shows such intensity cross-sectional images at sixteen equally spaced vertical positions. The top left picture shows the image of our circuit when it is closest to the objective, while the bottom right picture is the one when the circuit is farthest from the objective during the scan. As we scan along the  $z$ -axis [or equivalently moving across row by row in Fig. 11(a)], different regions of the circuit come into focus at different axial locations. Considering that the vertical separation between each picture is only  $0.137\text{ }\mu\text{m}$ , the range resolution of the MCM is superior with intensity images alone to that of a confocal microscope. As a by-product of the Fourier transform algorithm, we have the corresponding phase images shown in Fig. 11(b). Since the height variations in our integrated circuit are more than a wavelength, the phase images suffer from ambiguous  $2\pi$  phase wraparounds which make them hard to interpret.

#### IV. Conclusions

We have shown the advantages of using the Mirau interferometer configuration in an interference microscope. Such microscopes can measure both amplitude and phase. Only one microscope objective is used, and both the signal and reference beams pass through the same lens. This eliminates the complexity, vibration sensitivity due to the long path lengths, and cost of a system with two objectives. Furthermore, there is no problem of mismatch due to the use of different lenses, and aberrations in the range direction are removed.

The main drawback of a Mirau configuration is the aberration introduced by the beam splitter in front of the objective. This aberration is caused by the finite and uneven thickness of the beam splitter. We have produced a novel  $800\text{-}\text{\AA}$  thick silicon nitride film with a

uniformity of  $10\text{ }\text{\AA}$  by standard IC manufacturing technology and have thus minimized such aberrations.

The Mirau correlation microscope has been used to measure the widths and heights of various structures in integrated circuits. The results with amplitude measurements are very close to those obtained with the RSOM using the same filters and lens aperture. Phase measurements with this microscope are particularly useful for measuring small changes in height less than the range resolution of the microscope.

A disadvantage of this kind of microscope is the requirement for extensive electronic processing. However, as computers become progressively faster and more powerful, this disadvantage becomes less and less of a problem.

The authors would like to thank Tim Corle for many helpful discussions on the experiments and on the material in this paper. This work was supported by International business Machines Corp. contract 645416.

#### References

1. T. Wilson and C. J. R. Sheppard, *Theory and Practice of Scanning Optical Microscopy* (Academic, New York, 1984).
2. G. Q. Xiao, T. R. Corle, and G. S. Kino, "Real-Time Confocal Scanning Optical Microscope," *Appl. Phys. Lett.* **53**, 716-718 (1988).
3. M. Davidson, K. Kaufman, I. Mazor, and F. Cohen, "An Application of Interference Microscopy to Integrated Circuit Inspection and Metrology," *Proc. Soc. Photo-Opt. Instrum. Eng.* **775** (1987).
4. S. C. Chim, P. A. Beck, and G. S. Kino, "A Novel Thin Film Interferometer," submitted to *Rev. Sci. Instrum.* **61** (3), March 1990.
5. G. S. Kino and G. Q. Xiao, "Real-Time Scanning Optical Microscopes," *Scanning Optical Microscopes*, T. Wilson, Ed. (Pergamon, London, 1990).
6. P. A. Reinholdsten and B. T. Khuri-Yakub, "Confocal Imaging at Multiple Frequencies for Improved Depth Resolution," *J. Opt. Soc. America A* **7** in press.
7. J. W. Goodman, *Introduction to Fourier Optics* (McGraw-Hill, New York, 1968).
8. P. C. D. Hobbs and G. S. Kino, "Generalizing the Confocal Microscope via Heterodyne Interferometry and Digital Filtering," *J. Microsc.* (1990).